Research Article

Facile synthesis of metal and alloy nanoparticles by ultrasound-assisted dealloying of metallic glasses

Yuan-Yun Zhao [1, 2, 5], Feng Qian [2, 4], Wenfeng Shen [3], Chengliang Zhao [1, 5], Jianguo Wang [1, 5], Chunxiao Xie [1,5], Fengling Zhou [1], Chuntao Chang [1, 5*], Yanjun Li [2, *]

[1]*Neutron Scattering Technical Engineering Research Center, School of Mechanical Engineering, Dongguan University of Technology, Dongguan 523808, China*

[2]*Department of Materials Science and Engineering, Norwegian University of Science and Technology, Trondheim 7491, Norway*

[3]*Ningbo Institute of Materials Technology and Engineering, Chinese Academy of Sciences, Ningbo 315201, China*

[4]*School of Materials Science and Engineering, Beijing Institute of Technology, 100081, Beijing, China*

[5]*Guangdong-Hong Kong-Macao Joint Laboratory for Neutron Scattering Science and Technology, Dongguan University of Technology, Dongguan, 523808, China*

Metal and alloy nanoparticles synthesized by chemical reduction have attracted increasing attention due to their superior physical, chemical, and biological properties. However, most chemical synthesis processes rely on the use of harsh reducing agents and complicated chemical ingredients. Herein, we report a novel reduction-agent-free and surfactant (stabilizer)-free strategy to synthesize Cu, Ag, Au, Cu-Pt, Cu-Au, Cu-Au-Pt-Pd, and Au-Pt-Pd-Cu nanoparticles by ultrasound-assisted dealloying of Mg-based metallic glasses. The formation mechanism of the metal and alloy nanoparticles is revealed by a detailed investigation of sequential intermediate products. We demonstrate that the glass-liquid phase transition of the initially dealloying metallic glasses, together with the synergistic effect of dealloying and ultrasound-driven ligament-breakage of small enough nanoporous intermediates, play key roles in preparing the uniformly dispersed metal and alloy nanoparticles. This approach greatly simplifies the up-scaling synthesis of monometallic and bimetallic nanoparticles, and also provides a general strategy for synthesizing unprecedented multimetallic nanoparticles.

*Corresponding authors.

Email address: changct@dgut.edu.cn (C.T. Chang); yanjun.li@ntnu.no (Y.J. Li)

Key words: Metallic glasses; Dealloying; Ultrasound; Nanoparticles; Multimetallic nanoparticles

1. Introduction

Metal nanoparticles have attracted increasing research attention due to their remarkable size-dependent physical, chemical, and biological properties [1-4]. During the past decades, a variety of metal nanoparticles, such as Cu, Au, Ag, Pt, and Pd, have been produced with well-controlled morphologies and properties by different chemical reduction methods, in which the target metal ions in solution are reduced into nanoscale metallic clusters or aggregates [1,5-8]. However, the complexity of the chemical ingredients, the necessity of high-temperature reactions for burst nucleation, the contamination of metal nanoparticles by organic surfactants or stabilizers (such as polyvinylpyrrolidone (PVP) and hexadecyl trimethyl ammonium bromide (CTAB)), the use of toxic reducing agents (such as hydrazine, sodium borohydride ($NaBH_4$) and dimethyl formamide), and the production of chemical waste are still challenges for most chemical reduction methods [9-11]. In addition to controlling the morphological features and properties of monometallic nanoparticles, recent research has also focused on the fabrication of alloy nanoparticles with tuneable properties for diverse applications [4,12-15]. The addition of extra metal(s) into the metal nanoparticles is expected to produce synergistic effects between different metal elements, resulting in dramatic improvement in important physical and (or) chemical properties that outclass their counterpart monometallic nanoparticles in many aspects [12-16]. In the last decades, different solution-based synthetic methods, such as coreduction, thermal decomposition, galvanic replacement reactions, noble metal-induced reduction reactions, and seed-mediated growth, have been developed to synthesize various bimetallic and multimetallic nanoparticles [13,16,17]. However, synthesis of bimetallic and multimetallic nanoparticles with desired morphologies and composition is still challenging due to the difficulties in controlling the nanoparticle nucleation/growth kinetics in the presence of multiple

metal precursors with different reduction potentials. As a result, the one-step coreduction process of bimetallic or multimetallic precursors usually yields a mixture of monometallic nanoparticles [16,17]. The galvanic replacement and the seed-mediated sequential reduction methods have shown the potential to produce bimetallic and multimetallic nanoparticles with desired sizes and shapes. Unfortunately, these methods usually require stringent experimental conditions which are difficult to generalize, and thus necessitate tedious multistep reactions [12-17]. Although a few recently proposed methods, such as the carbothermal shock method [18], the template method using phenylazomethine dendrimers [19], the fast moving bed pyrolysis strategy [20], and the "sparking mashup" method [21], are effective in producing multimetallic nanoparticles of high quality and good monodispersity, they either need complex reagents and (or) equipment, harsh reaction conditions and multistep procedures, or are only suitable for sub-gram quantity production in lab scale. Therefore, development of more generalized and simple strategies for synthesis of monometallic, bimetallic, and multimetallic nanoparticles with controlled size and composition from inexpensive and non-toxic reactants is extremely desirable to meet the growing demand for metal and alloy nanoparticles in various applications.

As another widely used approach for synthesis of metallic nanomaterials, dealloying has been used as an effective and facile method to prepare nanoporous metals with intriguing physical, chemical, and mechanical properties [22-25]. During dealloying, the less noble metal is selectively removed from the precursor alloy, while atoms of the more noble metal diffuse and re-organize into a well-defined three-dimensional bi-continuous structure composed of nanoscale ligaments/pores [22]. To date, many nanoporous metals (e.g., Co, Cu, Ag, Au, Pt, and Pd) have been prepared by dealloying various crystalline precursor alloys [22-27] or metallic glass

precursors [28-33]. However, to the best of our knowledge, the dealloying approach has not been reported so far for the facile preparation of uniformly dispersed metal and alloy nanoparticles.

In this work, we report a novel ultrasound-assisted dealloying approach to prepare a variety of Cu, Ag, Au, Cu-Pt, Cu-Au, Cu-Au-Pt-Pd, and Au-Pt-Pd-Cu nanoparticles using Mg-Cu/Ni(Ag, Au, Pt, Pd)-Gd metallic glass ribbons. The present dealloying approach does not involve the reduction of target metal atoms from metal ions. Thus, reducing agents, surfactants, and stabilizers are not required to control the nucleation and growth of the metal and alloy nanoparticles. In chemical reduction methods, the composition of the alloy nanopaticles is controlled by the feed ratio of the precursors, whereas in this method the composition and size of the metal and alloy nanoparticles can be controlled by simply tuning the composition of the metallic glass precursors. This greatly simplifies the preparation of alloy nanoparticles, especially for multimetallic nanoparticles with more than three components. The formation mechanism of the metal and alloy nanoparticles is revealed by a detailed investigation of the intermediate products formed in different stages of dealloying. It is found that the glass-liquid phase transition of the initially dealloying metallic glasses, together with the synergistic effect of dealloying and ultrasound-driven ligament-breakage of the nanoporous intermediates, play key roles in preparing the uniformly dispersed metal and alloy nanoparticles. The present study offers a unique strategy for design and synthesis of a variety of monometallic, bimetallic and especially multimetallic nanoparticles.

2. Experimental

$Mg_{61}Cu_{28}Gd_{11}$, $Mg_{61}Ni_7Ag_{21}Gd_{11}$, $Mg_{61}Cu_{25}Pt_3Gd_{11}$, $Mg_{61}Cu_{21}Au_7Gd_{11}$, and $Mg_{61}Cu_{21}Au_5Pt_1Pd_1Gd_{11}$ (at.%) alloy ingots were prepared by induction melting mixtures of pure

Mg (>99.95 wt.%), Cu (>99.95 wt.%), Ni (>99.95 wt.%), Ag (>99.95 wt.%), Au (>99.95 wt.%), Pt (>99.95 wt.%), Pd (>99.95 wt.%), and Gd (>99.9 wt.%) metals in an argon atmosphere. By remelting the master alloy ingots, $Mg_{61}Cu_{28}Gd_{11}$, $Mg_{61}Ni_7Ag_{21}Gd_{11}$, $Mg_{61}Cu_{25}Pt_3Gd_{11}$, $Mg_{61}Cu_{21}Au_7Gd_{11}$, and $Mg_{61}Cu_{21}Au_5Pt_1Pd_1Gd_{11}$ metallic glass ribbons with thicknesses of 20-30 μm were prepared by a single copper roller melt-spinning process. Crystalline $Mg_{61}Cu_{28}Gd_{11}$ ribbons were prepared by annealing the $Mg_{61}Cu_{28}Gd_{11}$ metallic glass ribbons at 400 ℃ for 45 min.

In typical synthesis procedures, 0.25 g $Mg_{61}Cu_{28}Gd_{11}$, $Mg_{61}Ni_7Ag_{21}Gd_{11}$, $Mg_{61}Cu_{25}Pt_3Gd_{11}$, $Mg_{61}Cu_{21}Au_7Gd_{11}$, and $Mg_{61}Cu_{21}Au_5Pt_1Pd_1Gd_{11}$ metallic glass ribbons were added into 30 ml, 40 ml, 37 ml, 33 ml, and 31 ml of HCl/ethanol solution (0.24 mol L^{-1}) at room temperature, respectively. The dealloying processes were synchronously assisted by ultrasound that was generated by a common ultrasonic cleaning machine with an ultrasonic intensity of ~4 kW m^{-2}. The ultrasound-assisted dealloying processes lasted 90 min. Four sequential intermediate products sampled at 2 min, 5 min, 20 min, and 45 min were collected by ultrasound-assisted dealloying of $Mg_{61}Cu_{28}Gd_{11}$ metallic glass ribbons. For the synthesis of Au and Au-Pt-Pd-Cu nanoparticles, 0.25 $Mg_{61}Cu_{21}Au_7Gd_{11}$ and $Mg_{61}Cu_{21}Au_5Pt_1Pd_1Gd_{11}$ metallic glass ribbons were ultrasound-assisted dealloyed by 35 ml and 31 ml of HCl/ethanol solutions (0.24 mol L^{-1}) at room temperature for 90 min, respectively. Then, the Cu-Au and Cu-Au-Pt-Pd colloidal solutions containing residual HCl were left standing for 10 days to further slowly reduce the Cu content in the Cu-Au and Cu-Au-Pt-Pd nanoparticles and to modify their morphologies. All of the resulting colloidal solutions were centrifuged and washed with deaerated ethanol two times at 12000 rpm for 10 min and then kept for further experiments. To investigate the influence of ultrasound treatment on the products, nanoporous Cu, Ag, Cu-Pt, Cu-Au, and Cu-Au-Pt-Pd were

also prepared by ordinary dealloying of 0.25 g $Mg_{61}Cu_{28}Gd_{11}$, $Mg_{61}Ni_7Ag_{21}Gd_{11}$, $Mg_{61}Cu_{25}Pt_3Gd_{11}$, $Mg_{61}Cu_{21}Au_7Gd_{11}$, and $Mg_{61}Cu_{21}Au_5Pt_1Pd_1Gd_{11}$ metallic glass ribbons in 30 ml, 40 ml, 37 ml, 33 ml, and 31 ml of HCl/ethanol solution (0.24 mol L^{-1}) at room temperature, respectively.

The morphologies of the intermediate products and the as-prepared products were characterized by scanning electron microscopy (SEM) equipped with energy dispersive X-ray spectroscopy (EDS). Transmission electron microscopy (TEM), high resolution transmission electron microscopy (HRTEM), selected area electron diffraction (SAED), energy-dispersive X-ray spectroscopy (EDS), scanning transmission electron microscopy (STEM), and spectral maps were obtained by JEOL 2100 F. The crystal structures of the samples were examined using a Bruker D8 Advance X-ray diffractometer with Cu K_a radiation (λ = 0.1542 nm). The glass transition temperature of the precursor alloys was investigated by differential scanning calorimetry (DSC) at a heating rate of 20 K min^{-1}.

3. **Results and Discussion**

3.1. Synthesis and characterization of metal and alloy nanoparticles

Mg-Cu/Ni(Ag, Au, Pt, Pd)-Gd metallic glass ribbons ($Mg_{61}Cu_{28}Gd_{11}$, $Mg_{61}Ni_7Ag_{21}Gd_{11}$, $Mg_{61}Cu_{25}Pt_3Gd_{11}$, $Mg_{61}Cu_{21}Au_7Gd_{11}$, and $Mg_{61}Cu_{21}Au_5Pt_1Pd_1Gd_{11}$) with thicknesses of 20-30 μm were used as precursor materials to synthesize different metal and alloy nanoparticles (Fig. 1a). Here, with a high glass-forming ability, the Mg-Cu/Ni-Gd alloys can be easily made into metallic glass precursor ribbons by melt spinning method [34,35]. By partially substituting Cu or Ni with other target metal elements (such as Ag, Au, Pt, and Pd), a variety of multicomponent

metallic glass precursor ribbons can be designed and prepared for synthesis of different bimetallic and multimetallic nanoparticles. The amorphous structure of the metallic glass precursor ribbons was confirmed by X-ray diffraction (XRD) (Supplementary Fig. 1). Based on the target composition of each product, a certain amount of 0.24 mol/L HCl/ethanol solution was used as the corrosive solution. The dealloying processes were assisted by ultrasonic treatment (UT) with an ultrasound intensity of ~4 kW/m^2 and a frequency of 40 kHz (Fig. 1a). Taking the synthesis of Cu nanoparticles as an example, red-brown colloidal Cu nanoparticles can be synthesized by ultrasound-assisted dealloying of $Mg_{61}Cu_{28}Gd_{11}$ metallic glass ribbons for 90 min (Supplementary Fig. 2). Without using any surfactant or stabilizer, the as-prepared colloidal Cu nanoparticles exhibits a strong resistance to sedimentation, where only soft aggregation can be observed after sanding for 5h (Fig. 1b). However, they can be easily re-dispersed by a subsequent ultrasonic dispersion process (Supplementary Fig. 3). Through the same procedure, monometallic Ag, bimetallic Cu-Pt and Cu-Au, and multimetallic Cu-Au-Pt-Pd nanoparticles were also synthesized by ultrasound-assisted dealloying of $Mg_{61}Ni_7Ag_{21}Gd_{11}$, $Mg_{61}Cu_{25}Pt_3Gd_{11}$, $Mg_{61}Cu_{21}Au_7Gd_{11}$, and $Mg_{61}Cu_{21}Au_5Pt_1Pd_1Gd_{11}$ metallic glass ribbons, respectively (Fig. 1c-f). Their colloidal solutions also show a strong resistance to sedimentation. As shown in Fig. 1e and f, no obvious sedimentation and stratification can be observed for the colloidal Cu-Au and Cu-Au-Pt-Pd nanoparticles after standing for 24 h. Moreover, it is also found that the morphologies and composition of the as-prepared bimetallic or multimetallic nanoparticles can be easily modified by further dissolving of the relatively less noble element(s) in the bimetallic or multimetallic nanoparticles. For example, here Au and Au-Pt-Pd-Cu nanoparticles can be prepared by further dissolving all or part of Cu in the colloidal Cu-Au and Cu-Au-Pt-Pd nanoparticles, respectively (Fig. 1g and h). This process is also accompanied by a controllable

coalescence and growth of the Au and Au-Pt-Pd-Cu nanoparticles, resulting in the increase of the particle size. Details of the synthesis procedures for the Cu, Ag, Cu-Pt, Cu-Au, Cu-Au-Pt-Pd, Au, and Au-Pt-Pd-Cu nanoparticles can be found in the Methods section and the Supplementary Information.

Figure 2 shows representative transmission electron microscopy (TEM) images and size distribution histograms of the as-prepared metal and alloy nanoparticles. The as-prepared Cu, Ag, Cu-Pt, Cu-Au, Cu-Au-Pt-Pd, Au, and Au-Pt-Pd-Cu nanoparticles have spherical shapes and average diameters of ~24 nm, ~41 nm, ~4.0 nm, ~3.0 nm, ~6.0 nm, ~21 nm, and ~12 nm, respectively. High-resolution TEM images (Fig. 2a-g) showed that the lattice spacing of the representative Cu, Ag, Cu-Pt, Cu-Au, Cu-Au-Pt-Pd, Au, and Au-Pt-Pd-Cu nanoparticles is 0.206 nm, 0.204 nm, 0.215 nm, 0.220 nm, 0.216 nm, 0.236 nm, and 0.231 nm, respectively, which are corresponding to the (111), (200), (111), (111), (111), (111), and (111) planes of their face-centred cubic (fcc) lattices, respectively. Based on the energy-dispersive spectroscopy (EDS) results (Supplementary Fig. 4), the average composition (at.%) of the as-prepared Cu, Ag, Cu-Pt, Cu-Au, Cu-Au-Pt-Pd, Au, and Au-Pt-Pd-Cu nanoparticles are Cu, Ag, $Cu_{68}Pt_{32}$, $Cu_{48}Au_{52}$, $Cu_{70}Au_{22}Pt_4Pd_4$, Au, and $Au_{67}Pt_{12}Pd_{11}Cu_{10}$, respectively. By comparing the composition of these metal and alloy nanoparticles with their corresponding metallic glass precursors, it can be found that part of the Cu content in the $Mg_{61}Cu_{25}Pt_3Gd_{11}$, $Mg_{61}Cu_{21}Au_7Gd_{11}$, and $Mg_{61}Cu_{21}Au_5Pt_1Pd_1Gd_{11}$ metallic glass ribbons were also dissolved by dealloying. These results are consistent with our design, in which the volume of the reaction solutions and the corresponding H^+ content were specifically calculated to control the Cu content (nanoscale Cu can slowly react with dilute H^+) in the target alloy nanoparticles. Since nanoscale Au, Pt, and Pd do not react with dilute H^+, the molar ratio of C_{Au}:C_{Pt}:C_{Pd} in the as-prepared Cu-Au-Pt-Pd

nanoparticles can be well controlled by the composition design of the metallic glass precursors. For example, here the measured molar ratios of C_{Au}:C_{Pt}:C_{Pd} in the $Cu_{70}Au_{22}Pt_4Pd_4$ and $Au_{67}Pt_{12}Pd_{11}Cu_{10}$ nanoparticles are 5.5 : 1 : 1 and 5.6 : 1 : 0.9, respectively, which are almost the same as that in the corresponding $Mg_{61}Cu_{21}Au_5Pt_1Pd_1Gd_{11}$ metallic glass ribbons.

Figure 3a shows the powder XRD spectra of the as-prepared Cu, Ag, Au, Cu-Pt, Cu-Au, Cu-Au-Pt-Pd, and Au-Pt-Pd-Cu nanoparticles. For comparison, the XRD spectra of pure Cu, Au, Ag, and Pt are also presented. In each XRD spectrum, only one single fcc phase is determined, indicating that the as-prepared Cu-Pt, Cu-Au, Cu-Au-Pt-Pd, and Au-Pt-Pd-Cu samples are composed of bimetallic or multimetallic nanoparticles. Specifically, the bimetallic Cu-Pt (or Cu-Au) alloy phase is evidenced by the (111), (200), (220), and (311) reflections located between the reflections of pure Pt (or Au) and pure Cu fcc phase, indicating lattice contraction due to insertion of the Cu atoms into the Pt (or Au) lattice. The high intensity, broad XRD reflection peaks at ~41.9° in the Cu-Pt sample and ~40.9° in the Cu-Au sample are in good agreements with the (111) lattice planes of fcc Cu-Pt and Cu-Au alloys, respectively [36]. The interplanar spacing calculated from the scattering angle of the (111) diffraction peaks is 0.216 nm and 0.222 nm for the Cu-Pt and Cu-Au samples, respectively. These results are consistent with the high-resolution TEM (HRTEM) observation of single Cu-Pt and Cu-Au nanoparticles (Fig. 2). According to the Vegard's law [37], the calculated compositions of the as-prepared Cu-Pt and Cu-Au samples are $Cu_{65}Pt_{35}$ and $Cu_{45}Au_{55}$, respectively, which is also consistent with the EDS results. The mean particle diameter of the as-prepared metal nanoparticles is also calculated from the XRD spectra using the Scherrer equation [38]. The calculated average particle diameters of the Cu, Ag, Cu-Pt, Cu-Au, Cu-Au-Pt-Pd, Au, and Au-Pt-Pd-Cu nanoparticles are ~22 nm, ~35 nm, ~4 nm, ~4 nm, ~5 nm, ~23 nm, and ~9 nm, respectively, which agree well with the results

measured by the TEM images (Fig. 2). Figure 3d-g shows the elemental maps of the $Au_{67}Pt_{12}Pd_{11}Cu_{10}$ nanoparticles obtained by scanning transmission electron microscopy coupled with energy-dispersive X-ray spectroscopy (STEM-EDS). These results demonstrate a homogeneous distribution of Au, Pt, Pd, and Cu atoms in the nanoparticles, further confirming the successful preparation of Au-Pt-Pd-Cu multimetallic nanoparticles.

3.2. Formation mechanism

To explore the formation mechanism of the metal and alloy nanoparticles, the morphology and composition of four sequential intermediate products (sampled after a reaction time of 2 min, 5 min, 20 min, and 45 min) during ultrasound-assisted dealloying of $Mg_{61}Cu_{28}Gd_{11}$ metallic glass ribbons were investigated (Fig. 4a-h). After dealloying for 2 min, the sample mainly consisted of remaining metallic glass ribbons (Fig. 4a-b) and partly dealloyed intermediate fragments that were peeled off from the outer layers of the corresponding remaining metallic glass ribbons (Fig. 4c-d). For the remaining metallic glass ribbons, as marked by the arrows in Fig. 4a-b, some traces of local "melting" can be observed on the outer surface and in the interior of the remaining ribbons. Considering that the glass transition temperatures (T_g) of the Mg-Cu/Ni(Ag, Au, Pt, Pd)-Gd metallic glasses are as low as 149-165 °C (Fig. 4i), it is speculated that the local temperature at the reaction sites may have exceeded the T_g, thus glass-liquid phase transition occurred during dealloying and the metallic glass around the reaction sites was actually in a supercooled liquid state [33]. The average composition of the "melted" regions is measured to be $Mg_{59}Cl_5Cu_{26}Gd_{10}$ (Supplementary Fig. 5). The presence of Cl in the "melted" regions indicates that HCl in the solution has been mixed and reacted with the supercooled liquid phase in the dealloying ribbons, and most of the as-formed $MgCl_2$ and $GdCl_3$ are retained in it

(Supplementary Fig. 5). For the partly dealloyed intermediate fragments, they have a size ranging from ~5 μm to ~25 μm and show a rudimentary ligaments/pores structure (Fig. 4c-d). The average composition of the intermediate fragments is measured to be $Mg_{21}Cl_1Cu_{69}Gd_9$ (Supplementary Fig. 6), indicating a high erosion rate of Mg and Gd during the first 2 min. The XRD spectrum demonstrates that the intermediate fragments are composed of both Cu phase and remaining amorphous phase (Fig. 4j). After dealloying for 5 min, the intermediate fragments were further dealloyed and broken into much smaller nanoporous particles with a size less than ~2 μm (Fig. 4f). The nanoporous particles show an obviously ligaments/pores structure, in which the average size of the ligaments is ~25 nm (Fig. 4e). The average composition of the nanoporous particles is measured to be $Mg_8Cu_{88}Gd_4$ (Supplementary Fig. 7), still containing a considerable amount of Mg and Gd. After dealloying for 20 min, the TEM image and XRD spectrum show that the Cu-rich ligaments in the small nanoporous particles can be further broken into irregular nanorod-like ligament debris, and the size of the ligaments remain unchanged (Fig. 4g and j). The average composition of the ligament debris is measured to be $Mg_3Cu_{95}Gd_2$, which still contains a small amount of Mg and Gd (Supplementary Fig. 8). After dealloying for 45 min, the ligament debris can be further broken into spherical Cu nanoparticles with a diameter of 15-30 nm and a small fraction of short Cu nanorods with a length of 20-70 nm (Fig. 4h, Supplementary Fig. 8). After dealloying for 90 min, spherical Cu nanoparticles with an average diameter of ~24 nm were prepared (Fig. 2, Supplementary Fig. 8).

Figure 4k shows a plot of the average diameter of the as-prepared Cu, Ag, Cu-Pt, Cu-Au, and Cu-Au-Pt-Pd nanoparticles *vs*. the average diameter of ligaments in the corresponding nanoporous metals prepared by ordinary dealloying (without UT) of $Mg_{61}Cu_{28}Gd_{11}$, $Mg_{61}Ni_7Ag_{21}Gd_{11}$, $Mg_{61}Cu_{25}Pt_3Gd_{11}$, $Mg_{61}Cu_{21}Au_7Gd_{11}$, and $Mg_{61}Cu_{21}Au_5Pt_1Pd_1Gd_{11}$ metallic

glass ribbons, respectively. The average diameter of the ligaments in the nanoporous Cu, Ag, Cu-Pt, Cu-Au, and Cu-Au-Pt-Pd are ~27 nm, ~42 nm, ~3 nm, ~3 nm, and ~7 nm (Fig. 4k, Supplementary Fig. 9), respectively, which are almost the same as the average diameter of the corresponding metal and alloy nanoparticles. There is sufficient evidence to show that, with the assistance of UT, the formation of metal and alloy nanoparticle is related to the complete breakage of the ligaments in the corresponding nanoporous particles. Moreover, it is interesting to see that, by partially substituting Cu with Pt, Au, and Pd in the Mg-Cu-Gd metallic glass precursors, a significant decrease in the size of the ligaments and their corresponding Cu-Pt, Cu-Au, and Cu-Au-Pt-Pd nanoparticles are achieved by dealloying. So the size and composition of the metal and alloy nanoparticles can be controlled and manipulated by simply tuning the composition of the metallic glass precursors.

Based on the above experimental evidences, the formation mechanism of metal and alloy nanoparticles by ultrasound-assisted dealloying of metallic glass ribbons is schematically illustrated in Fig. 5 (taking the synthesis of Cu nanoparticles as an example). To be concise, we divide the formation process into three stages: (1) dealloying and breakage of the initial dealloyed Mg-Cu-Gd precursor ribbons (Fig. 5a-c), (2) dealloying and complete breakage of Cu-rich ligaments in intermediate nanoporous Cu-rich particles (Fig. 5c-e), and (3) spheroidization of the Cu nanoparticles (Fig. 5e-f). During the first stage, the reaction latent heat induced local temperature rose above the T_g and caused local glass-liquid transition of the precursor ribbons (Fig. 4i and 5b). Due to a low viscosity (η=10^6-10^8 Pa·s) of the supercooled liquid phase [39], the bulging effect of in-situ generated H_2 ($Mg + H^+ \rightarrow H_2 + Mg^{2+}$, $Gd + H^+ \rightarrow H_2 + Gd^{3+}$) on the supercooled liquid phase occurred not only on the surface regions but also in some interior regions of the precursor ribbons (Fig. 4b and 5b). As a result, loose biscuit-like nanoporous

ribbon fragments, rather than intact nanoporous ribbons that maintained their initial shape, formed even without UT (Supplementary Fig. 10). This morphology is totally different from that of the products by ordinary dealloying of similar $Mg_{65}Cu_{25}Y_{10}$ and $Mg_{65}Cu_{25}Gd_{10}$ metallic glass ribbons in H_2SO_4 aqueous solution, in which the as-formed nanoporous Cu maintained the shape of the initial precursor ribbons [29,30]. When the dealloying process is assisted with UT, the supercooled liquid phase in the dealloying precursor ribbons can be partly dealloyed and broken into small intermediate fragments (Fig. 5a-b). Subsequently, these intermediate fragments can be further dealloyed and broken into much smaller Cu-rich nanoporous particles with considerable amount of residual Mg and Gd (Fig. 5b-c). In the second stage, the remaining Cu atoms in the Cu-rich ligaments continue to diffuse and rearrange for further crystallization, while the residual Mg and Gd atoms are continuously dissolved. In view of the fact that the Cu-rich ligaments in the nanoporous particles are composed of nanopolycrystals, it can be expected that the diffusion and dissolving rate of atoms at the grain boundaries are faster than that in inner grains, which makes the grain boundaries mechanically and chemically unstable. One the other hand, the acoustic cavitation induced by ultrasonic wave can generate implosive bubble collapse and associated shock waves in the solution [40,41]. The shock waves can cause many physical effects, such as surface damage at the liquid-solid interfaces [42,43], dispersion of agglomerated powders [44], and particle breakage due to high-velocity interparticle collisions [41,45]. When the dealloying process is assisted with UT, the small Cu-rich nanoporous particles can be further broken into Cu-rich ligament debris or short nanorods by a synergistic effect of dealloying and ultrasound-driven ligament-breakage process (Fig. 5d-e). Finally, spherical Cu nanoparticles can be prepared by a spheroidization process to reduce their surface energy (Fig. 5e-f) [46].

3.3. Discussion

It is well known that the dealloying of precursor alloys usually leads to the formation of nanoporous metals with three-dimensional bi-continuous ligaments/pores. In this work, for the first time, highly dispersed metal and alloy nanoparticles can be prepared by an ultrasound-assisted dealloying approach. We propose that the following factors are crucial to achieve this breakthrough: (1) UT assisted dealloying, (2) metallic glass precursors with low T_g, (3) HCl/ethanol corrosive solution. Supplementary Fig. 11-14 present photographs of the products when one of the above conditions was not met. (I) The UT was performed after ordinary dealloying of $Mg_{61}Cu_{28}Gd_{11}$ metallic glass ribbons in HCl/ethanol solution (Supplementary Fig. 11), (II) ultrasound-assisted dealloying of crystalline $Mg_{61}Cu_{28}Gd_{11}$ ribbons in HCl/ethanol solution (Supplementary Fig. 12), and (III) ultrasound-assisted dealloying of $Mg_{61}Cu_{28}Gd_{11}$ metallic glass ribbons in HCl/water solution (Supplementary Fig. 13) or H_2SO_4/water solution (Supplementary Fig. 14). In all cases, the products are mainly large micro-sized nanoporous Cu particles that can not be further broken into uniformly dispersed Cu nanoparticles. Similar results have also been reported by ultrasound-assisted dealloying of crystalline Mg-Ag alloy in HCl/ethanol solution, in which micro-sized (30-110 μm) nanoporous Ag particles, rather than uniformly dispersed Ag nanoparticles, were prepared [27]. Based on these evidences, We speculated that there might be a critical particle size, below which the intermediate nanoporous particles can be accelerated to a critical velocity by ultrasonic waves. Thus, in addition to being directly triggered by acoustic cavitation, the complete breakage of ligaments in intermediate nanoporous particles can be further achieved by high-velocity interparticle collisions [41,45]. Considering that the supercooled liquid phase with low viscosity can be easily broken into small pieces by UT, we believed that the formation of small enough intermediate nanoporous particles

(with a size less than 2 μm) and the complete breakage of ligaments in small nanoporous particles are closely related to the glass-liquid transition of the precursor alloys during dealloying. While for the other cases mentioned above, the size of the intermediate nanoporous particles is tens of microns (Supplementary Fig. 11-14), which should have exceeded the critical particle size, and thus the complete breakage of ligaments in large intermediate nanoporous particles can not occur due to ineffective interparticle collisions with low-velocity. Besides the assistance of UT and the use of metallic glass precursors with low T_g, it is also found that the introduction of HCl/ethanol corrosive solution is also crucial for the synthesis of present metal and alloy nanoparticles (Supplementary Fig. 13-14). One the one hand, ethanol with lower thermal conductivity (λ = 0.18 W (m K)$^{-1}$) and heat capacity (C = 2.4 kJ (kg K)$^{-1}$) compared to water is beneficial to the accumulation of reaction latent heat, thus promoting the local temperature rise above T_g to induce local glass-liquid transition of the metallic glass precursors. One the other hand, ethanol instead of water can greatly slow down the reaction rate, so that the local temperature of the dealloying metallic glass precursors can not exceed their crystallization temperature (T_x = 195-205 ℃ , Fig. 4i). Therefore, the local temperature of the metallic glass around the reaction sites can be controlled between T_g and T_x, leading to a stable existence of supercooled liquid phase and thus facilitating the synergistic effect of dealloying and ultrasound-driven breakage processes. Third, because $GdCl_3$ and $MgCl_2$ are highly soluble (the solubility of $GdCl_3$ and $MgCl_2$ in ethanol at 298 K is about ~2.4 mol kg^{-1} and ~0.7 mol kg^{-1}, respectively) [47,48], while $MgSO_4$ and $Gd_2(SO_4)_3$ are insoluble in ethanol, HCl rather than H_2SO_4 is selected as the most suitable acid for dealloying (HNO_3 is also excluded because of its strong oxidability). Therefore, we propose that the synthesis of metal and alloy nanoparticles is also attributed to a synergistic effect of metallic glass precursors, HCl, ethanol, and UT in the dealloying system.

It is worth noting that the present synthesis process involves neither the nucleation and growth of metallic clusters from metallic ions nor the decrease in the size of the bulk metals or alloys to the nanoscale, so it cannot be simply classified as either conventional bottom-up or top-down approaches [49]. Moreover, here the less noble elements are chemically dissolved during dealloying, while the remaining ligaments with target noble elements are broken into metal nanoparticles by UT. Thus, the present method has the characteristics of both chemical and physical approaches. In comparison to traditional chemical synthesis approaches, one of the most distinguishing advantages of the present strategy is that it greatly simplifies the synthesis process of metal and alloy nanoparticles with controlled size and composition. On the one hand, without the requirement of reducing agents and stabilizers (or surfactants) to control the nucleation and growth of metallic clusters, the size of the metal and alloy nanoparticles can be well controlled by the size of the ligaments in the corresponding nanoporous metals, which is a fixed value for a given reaction system. On the other hand, the composition of the metal and alloy nanoparticles, especially multimetallic nanoparticles, can be well designed and easily controlled by the composition design of the precursor alloys. As a result, the synthesis of multimetallic nanoparticles containing several alloying elements like Cu, Ag, Au, Pt, Pd, Ir, Re, and Ru is possible by ultrasound-assisted dealloying of Mg-Cu/Ni(Ag-Au-Pt-Pd-Ir-Re-Ru)-Gd metallic glass precursors. Furthermore, in view of the facts that the reactants just simply consist of inexpensive Mg-based metallic glasses and a dilute HCl/ethanol solution, and the synthesis processes can be carried out at room temperature and atmospheric pressure, the present one-step preparation method is much simpler than most chemical synthesis methods consisting of complicated chemical ingredients and tedious multistep reactions. Without requiring harsh conditions and equipment, the present method is also more economical and feasible for up-

scaling production of multimetallic nanoparticles than other newly developed physical methods, such as the "sparking mashup" method [21].

4. Conclusion

In summary, a novel strategy to simplify the synthesis of metal and alloy nanoparticles by ultrasound-assisted dealloying of metallic glass ribbons was proposed. The formation mechanism of the metal and alloy nanoparticles is investigated by analysing the intermediate products formed at different synthesis stages. It is revealed that the glass-liquid phase transition of the initially dealloying metallic glasses, together with the synergistic effect of dealloying and ultrasound-driven ligament-breakage of small enough nanoporous intermediates, play key roles in preparing the present metal and alloy nanoparticles. With its simple and flexible nature, this synthesis strategy not only has a big potential for up-scaling industrial production of a variety of monometallic, bimetallic, and multimetallic nanoparticles with desired composition and properties, but also provides a new perspective for the application of metallic glasses.

Declaration of Competing Interest

None.

Acknowledgements

This work was financially supported by Guangdong Major Project of Basic and Applied Basic Research, China (No. 2019B030302010), the National Natural Science Foundation of China (Nos. 51671206 and 51871056), the foundation from the Department of Education of

Guangdong Province (No. 2018KZDXM069), and the Natural Science Foundation of Guangdong Province (No. 2019B030302010).

Appendix A. Supplementary data

Supplementary material related to this article can be found, in the online version, at doi:

References

[1] M.B. Gawande, A. Goswami, F.X. Felpin, T. Asefa, X.X. Huang, R. Silva, X.X. Zou, R. Zboril, R.S. Varma, Chem. Rev. 116 (2016) 3722-3811.

[2] F. Yan, L. Liu, T.R. Walsh, Y. Gong, P.Z. El-Khoury, Y. Zhang, Z. Zhu, J.J. De Yoreo, M.H. Engelhard, X. Zhang, C.-L, Chen, Nat. Commun. **9** (2018) 2327.

[3] N.L. Rosi, C.A. Mirkin, Chem. Rev. 105 (2005) 1547-1562.

[4] K.D. Gilroy, A. Ruditskiy, H.-C. Peng, D. Qin, Y. Xia, Chem. Rev. 116 (2016) 10414-10472.

[5] Y. Sun, Y. Xia. Science 298 (2002) 2176-2179.

[6] J. Yang, E.H. Sargent, S.O, Kelley, J.Y. Ying, Nat. Mater. 8 (2009) 683-689.

[7] X. Pang, L. Zhao, W. Han, X. Xin, Z. Lin, Nat. Nanotechnol. 8 (2013) 426-431.

[8] X. Wang, J. Zhuang, Q. Peng, Y. Li, Nature 437 (2005) 121-124.

[9] J. Singh, T. Dutta, K.-H. Kim, M. Rawat, P. Samddar, P. Kumar, J Nanobiotechnol 16 (2018) 84.

[10] J. Virkutyte, R.S. Varma, Chem. Sci. 2 (2011) 837-846.

[11] S. Iravani, Green Chem. 13 (2011) 2638-2650.

[12] Q. Zhang, J. Lee, J. Yang, C. Boothroyd, J. Zhang, Nanotechnology 18 (2007) 245605.

[13] G. Sharma, D. Kumar, A. Kumar, A.H. Al-Muhtaseb, D. Pathania, M. Naushad, G.T. Mola, Mater. Sci. Eng. C Mater. Biol. Appl. 71 (2017) 1216-1230.

[14] C. Tan, Y. Sun, J. Zheng, D. Wang, Z. Li, H. Zeng, J. Guo, L. Jing, L. Jiang, *Sci. Rep.* **7**, 6347 (2017).

[15] J.-X. Kang, T.-W. Chen, D.-F. Zhang, L. Guo, Nano Energy 23 (2006) 145-152.

[16] D. Wang, Y. Li, Adv. Mater. 23 (2011) 1044-1060.

[17] R. Ferrando, J. Jellinek, R.L. Johnston, Chem. Rev. 108 (2008) 845-910.

[18] Y. Yao, Z. Huang, P. Xie, S.D. Lacey, R.J. Jacob, H. Xie, F. Chen, A. Nie, T. Pu, M. Rehwoldt, D. Yu, M.R. Zachariah, C. Wang, R. Shahbazian-Yassar, J. Li, L. Hu, Science 359 (2018) 1489-1494.

[19] T. Tsukamoto, T. Kambe, A. Nakao, T. Imaoka, K. Yamamoto, Nat. Commun. 9 (2018) 3873.

[20] S. Gao, S. Hao, Z. Huang, Y. Yuan, J. Lu, Nat. Commun. 11 (2020) 2016.

[21] J. Feng, D. Chen, P.V. Pikhitsa, Y. Jung, J. Yang, M. Choi, Matter 3 (2020) 1-18.

[22] J. Erlebacher, M.J. Aziz, A. Karma, N. Dimitrov, K. Sieradzki, Nature 410 (2001) 450-453.

[23] J. Zhang, C.M. Li, Chem. Soc. Rev. 41 (2012) 7016-7031.

[24] Q. Chen, Y. Ding, M.W. Chen, MRS Bull. 43 (2018) 43-48.

[25] Z. Lu, C. Li, J. Han, F. Zhang, M. Chen, Nat. Commun. 9 (2018) 276.

[26] Z. Zhang, Y. Wang, Z. Qi, W. Zhang, J. Qin, J. Frenzel, J. Phys. Chem. C 113 (2009) 12629-12636.

[27] Y.-Y. Zhao, D. Estévez, C. Chang, H. Men, X. Wang, R.W. Li, Mater. Lett. 144 (2015) 138-141.

[28] J.Wang, X. Liu, R. Li, Z. Li, X. Wang, H. Wang, Y. Wu, S. Jiang, Z. Lu, Inorg. Chem. Front., 7 (2020) 1127-1139.

[29] Z. Deng, C. Zhang, L. Liu, Intermetallics 52 (2014) 9-14.

[30] X. Luo, R. Li, Z. Liu, L. Huang, M. Shi, T. Xu, T. Zhang, Mater. Lett. 76 (2012) 96-99.

[31] D. Ma, Y. Wang, Y.Li, R.Y. Umetsu, S. Ou, K. Yubuta, W. Zhang, J. Mater. Sci. Technol. 36 (2020) 128-133.

[32] J. Yu, Y. Ding, C. Xu, A. Inoue, T. Sakurai, M. Chen, Chem. Mater. 20 (2008) 4548-4550.

[33] Y.-Y. Zhao, F. Qian, C. Zhao, C. Xie, J. Wang, C. Chang, Y. Li, L.-C. Zhang, J. Mater. Sci. Technol. 70 (2021) 205-213.

[34] Q. Zheng, J. Xu, E. Ma, J. Appl. Phys. 102 (2007) 113519.

[35] Y. Li, H.Y. Liu, H. Jones, J. Mat. Sci. 31 (1996) 1857-1863.

[36] Y. Jia, J. Su, Z. Chen, K. Tan, Q. Chen, Z. Cao, Y. Jiang, Z. Xie, L. Zheng, RSC Adv. 5 (2015) 18153.

[37] A.R. Denton, N.W. Ashcroft, Phys. Rev. A 43 (1991) 3161-3164.

[38] B.D. Cullity, Elements of X-ray Diffraction (Addison-Wesley, Reading, Mass, USA, 2nd edition, 1978).

[39] R. Busch, J. Schroers, W.H. Wang, MRS Bull. 32 (2011) 620-623.

[40] K.S. Suslick, Science 247 (1990) 1439-1445.

[41] S.J. Doktycz, K.S. Suslick, Science 247 (1990) 1067-1069.

[42] Y. Ichida, R. Sato, Y. Morimoto, K. Kobayashi, Wear 258 (2005) 107-114.

[43] K.S. Suslick, G.J. Price, Ann. Rev. Mater. Sci. 29 (1999) 295-326.

[44] S.G. Thoma, M. Ciftcioglu, D.M. Smith, Powder Technol. 68 (1991)53-61.

[45] K.S. Suslick, D.J. Casadonte, M.L.H. Green, M.E. Thompson, Ultrasonics 25 (1987) 56-59.

[46] N. Wang, Y. Pan, S. Wu, J. Mat. Sci. Technol. 34 (2018) 1162-1171.

[47] L. Zeng, Z. Li, X. Wang, J. Chem. Eng. Data 61 (2016) 797-805.

[48] A. Merbach, M.N. Pitteloud, P. Jaccard, Helv. Chim. Acta 55 (1972) 44-52.

[49] S. Verma, R. Gokhale, D.J. Burgess, Int. J. Pharm. 380 (2009) 216-222.

Figure captions

Fig. 1. Synthesis of metal and alloy nanoparticles by ultrasound-assisted dealloying of Mg-Cu/Ni (Ag, Au, Pt, Pd)-Gd metallic glass ribbons. (a) Typical synthetic procedure to prepare metal and alloy nanoparticles by ultrasound-assisted dealloying metallic glass ribbons. (b-f) Photographs of as-prepared colloidal Cu (after standing for 5 h), Ag (after standing for 2 h), Cu-Pt (after standing for 24 h), Cu-Au (after standing for 24 h), and Cu-Au-Pt-Pd (after standing for 24 h) nanoparticles, respectively. (g-h) Photographs of colloidal Au (after standing for 10 days) and Au-Pt-Pd-Cu (after standing for 10 days) nanoparticles prepared by further dealloying of colloidal Cu-Au and Cu-Au-Pt-Pd nanoparticles, respectively.

Fig. 2. TEM images and size distributions of metal nanoparticles. (a1-g1, a2-g2) Representative low-magnification TEM images and high-magnification TEM images of Cu (a1, a2), Ag (b1, b2), Cu-Pt (c1, c2), Cu-Au (d1, d2), Cu-Au-Pt-Pd (e1, e2), Au (f1, f2), and Au-Pt-Pd-Cu (g1, g2) nanoparticles. (a3-g3) Size distribution histograms of Cu (a3), Ag (b3), Cu-Pt (c3), Cu-Au (d3), Cu-Au-Pt-Pd (e3), Au (f3), and Au-Pt-Pd-Cu (g3) nanoparticles.

Fig. 3. XRD spectra and elemental maps. (a) XRD spectra of the as-synthesized Cu, Ag, Au, Cu-Pt, Cu-Au, Cu-Au-Pt-Pd, and Au-Pt-Pd-Cu nanoparticles. The blue, brown, pink, and red vertical lines represent the reference peaks of pure Au, Pt, Ag, and Cu, respectively. (b-c) TEM and scanning TEM (STEM) images of typical Au-Pt-Pd-Cu nanoparticles, respectively. (d-g) STEM-

EDS elemental maps of the Au (d), Pt (e), Pd (f), and Cu (g) in typical Au-Pt-Pd-Cu nanoparticles.

Fig. 4. Evolution of the intermediate products by ultrasound-assisted dealloying $Mg_{61}Cu_{28}Gd_{11}$ metallic glass precursor ribbons. (a-b) SEM images of the outer surface (a) and cross section (b) of a metallic glass ribbon after dealloying for 2 min. (c-f) SEM images of the intermediate products after dealloying for 2 min (c-d) and 5 min (e-f). (g-h) TEM images of the intermediate products after dealloying for 20 min (g) and 45 min (h). (i) Differential scanning calorimetry (DSC) curves of the Mg-Cu/Ni (Ag, Au, Pt, Pd)-Gd metallic glasses. (j) XRD spectra of the intermediate products after dealloying for 2 min, 5 min, 20 min, 45 min, and 90 min. Due to the atmospheric oxidation during the preparation and test processes, a small amount of Cu_2O can be detected in the samples. (k) Mean diameter of metal and alloy nanoparticles *vs.* corresponding mean diameter of ligaments in nanoporous metals by dealloying Mg-Cu/Ni(Ag, Au, Pt, Pd)-Gd metallic glasses without UT. The inserts show SEM images of the corresponding nanoporous Cu and Cu-Au.

Fig. 5. Schematic illustration of the formation mechanism of Cu nanoparticles. (a) Metallic glass precursor ribbons. (b) Remaining metallic glass precursor ribbon and partly dealloyed intermediate fragments that were peeled off from the outer layers of the corresponding remaining metallic glass ribbons. The red regions represent the supercooled liquid regions ($T_g < T < T_x$) induced by the local glass transition. (c) Dealloying and breakage of intermediate fragments into small nanoporous Cu-rich particles. (d) Dealloying and breakage of small nanoporous Cu-rich

particles into Cu-rich ligament debris. (e) Dealloying and breakage of Cu-rich ligament debris into short Cu nanorods and Cu nanoparticles. (f) Spheroidization of Cu nanoparticles.

Figure list:

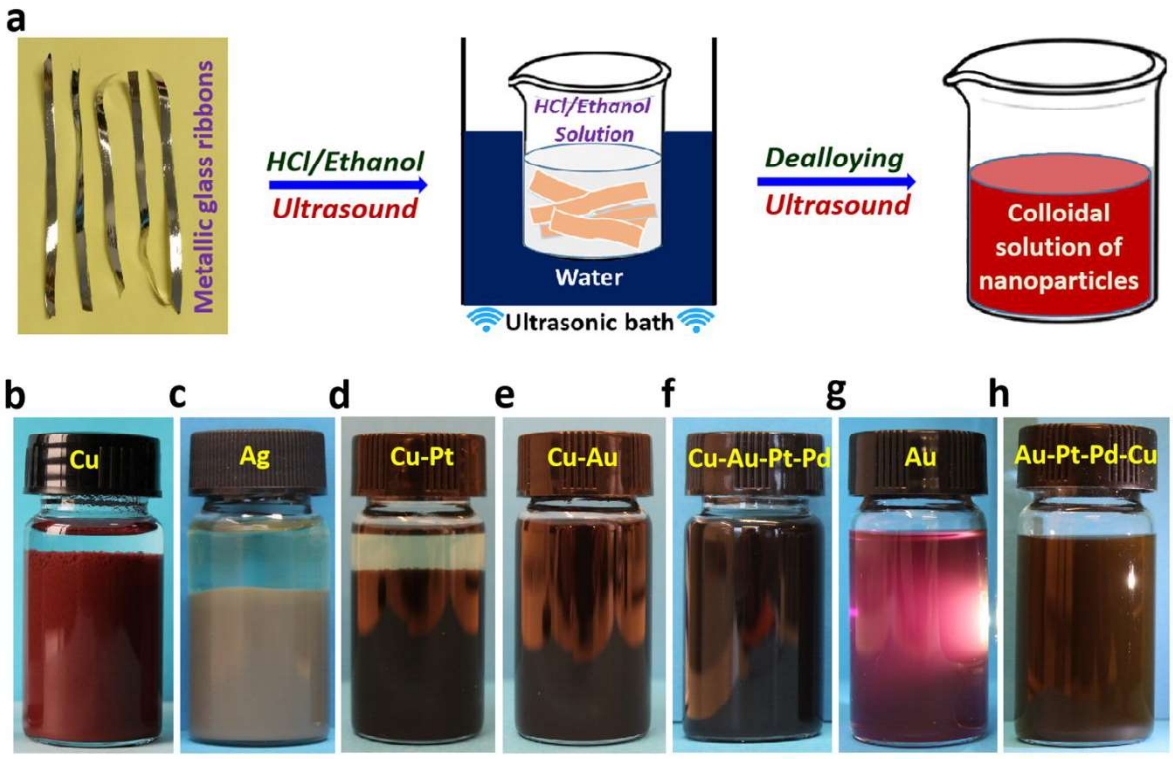

Figure 1

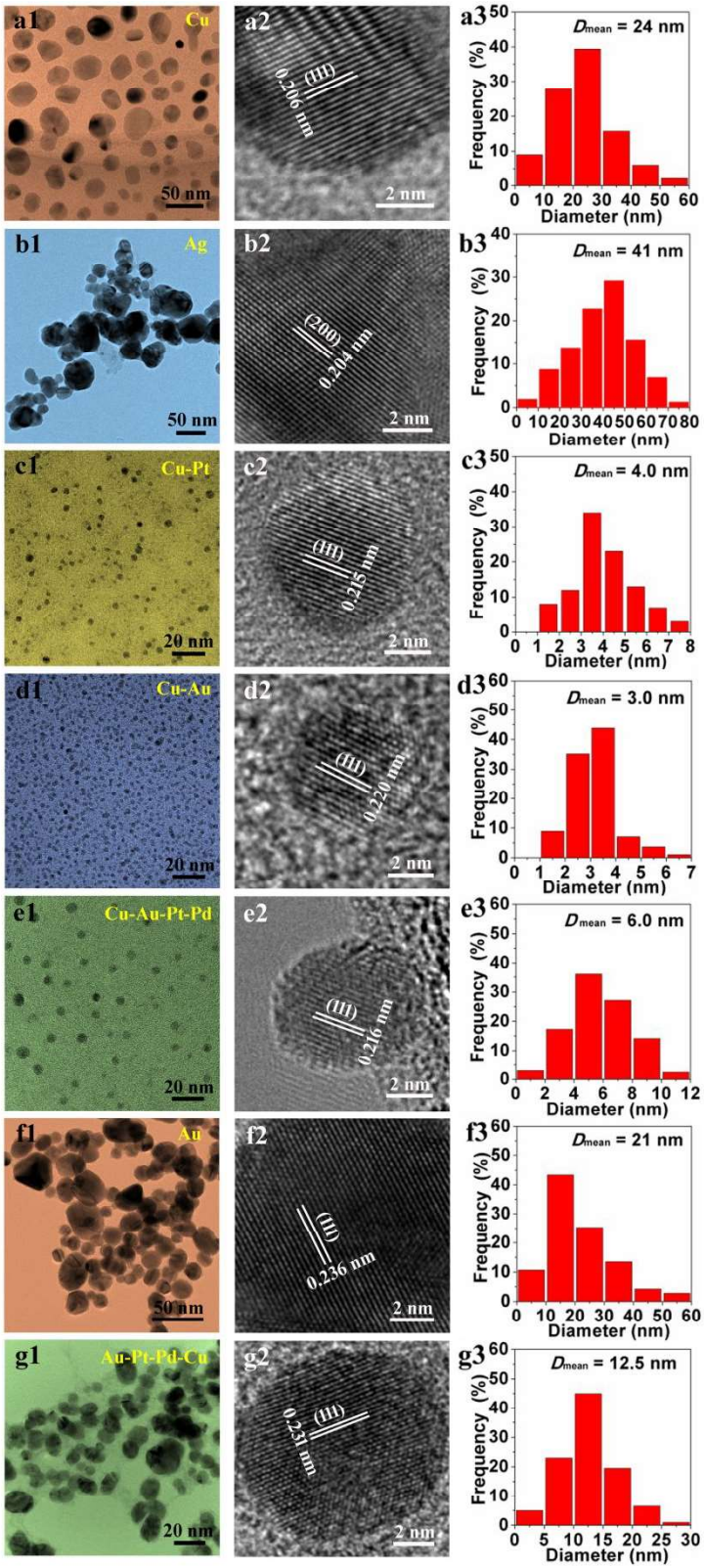
a1
Cu
50 nm
a2
(111)
0.206 nm
2 nm
a3
D_{mean} = 24 nm
Frequency (%)
Diameter (nm)
b1
Ag
50 nm
b2
(200)
0.204 nm
2 nm
b3
D_{mean} = 41 nm
Frequency (%)
Diameter (nm)
c1
Cu-Pt
20 nm
c2
(111)
0.215 nm
2 nm
c3
D_{mean} = 4.0 nm
Frequency (%)
Diameter (nm)
d1
Cu-Au
20 nm
d2
(111)
0.220 nm
2 nm
d3
D_{mean} = 3.0 nm
Frequency (%)
Diameter (nm)
e1
Cu-Au-Pt-Pd
20 nm
e2
(111)
0.216 nm
2 nm
e3
D_{mean} = 6.0 nm
Frequency (%)
Diameter (nm)
f1
Au
50 nm
f2
(111)
0.236 nm
2 nm
f3
D_{mean} = 21 nm
Frequency (%)
Diameter (nm)
g1
Au-Pt-Pd-Cu
20 nm
g2
(111)
0.231 nm
2 nm
g3
D_{mean} = 12.5 nm
Frequency (%)
Diameter (nm)

Figure 2

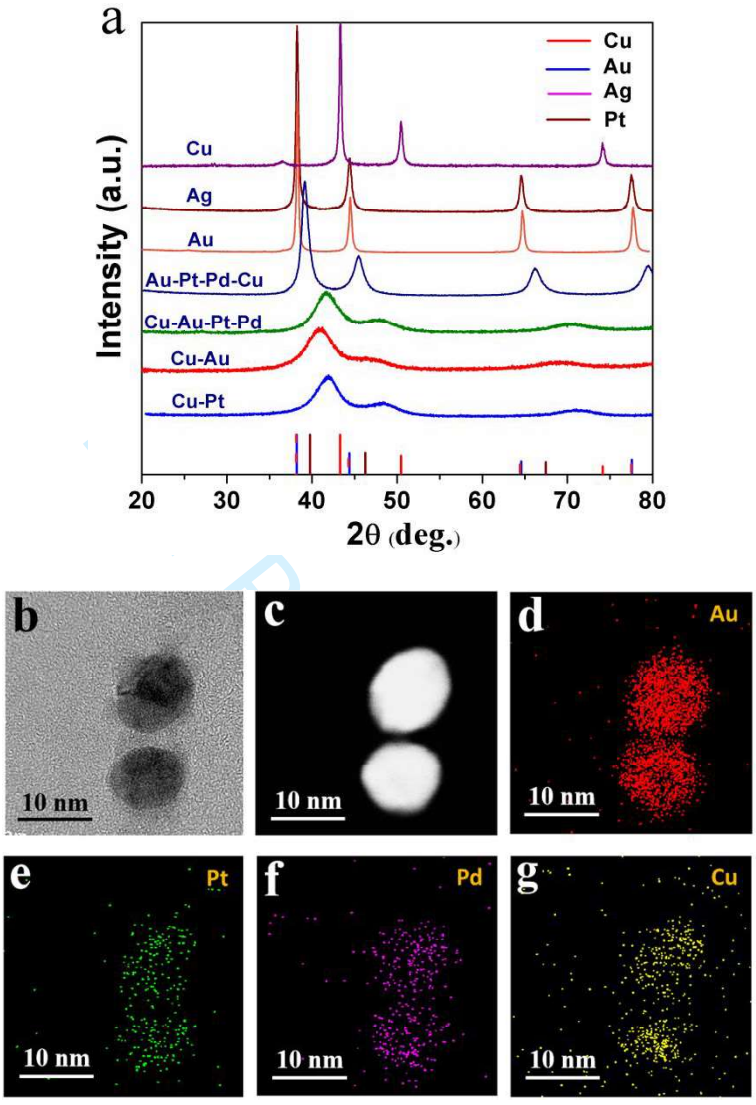
a
Cu
Au
Ag
Pt
Cu
Ag
Au
Au-Pt-Pd-Cu
Cu-Au-Pt-Pd
Cu-Au
Cu-Pt
Intensity (a.u.)
20
30
40
50
60
70
80
2θ (deg.)
b
10 nm
c
10 nm
d
Au
10 nm
e
Pt
10 nm
f
Pd
10 nm
g
Cu
10 nm

Figure 3

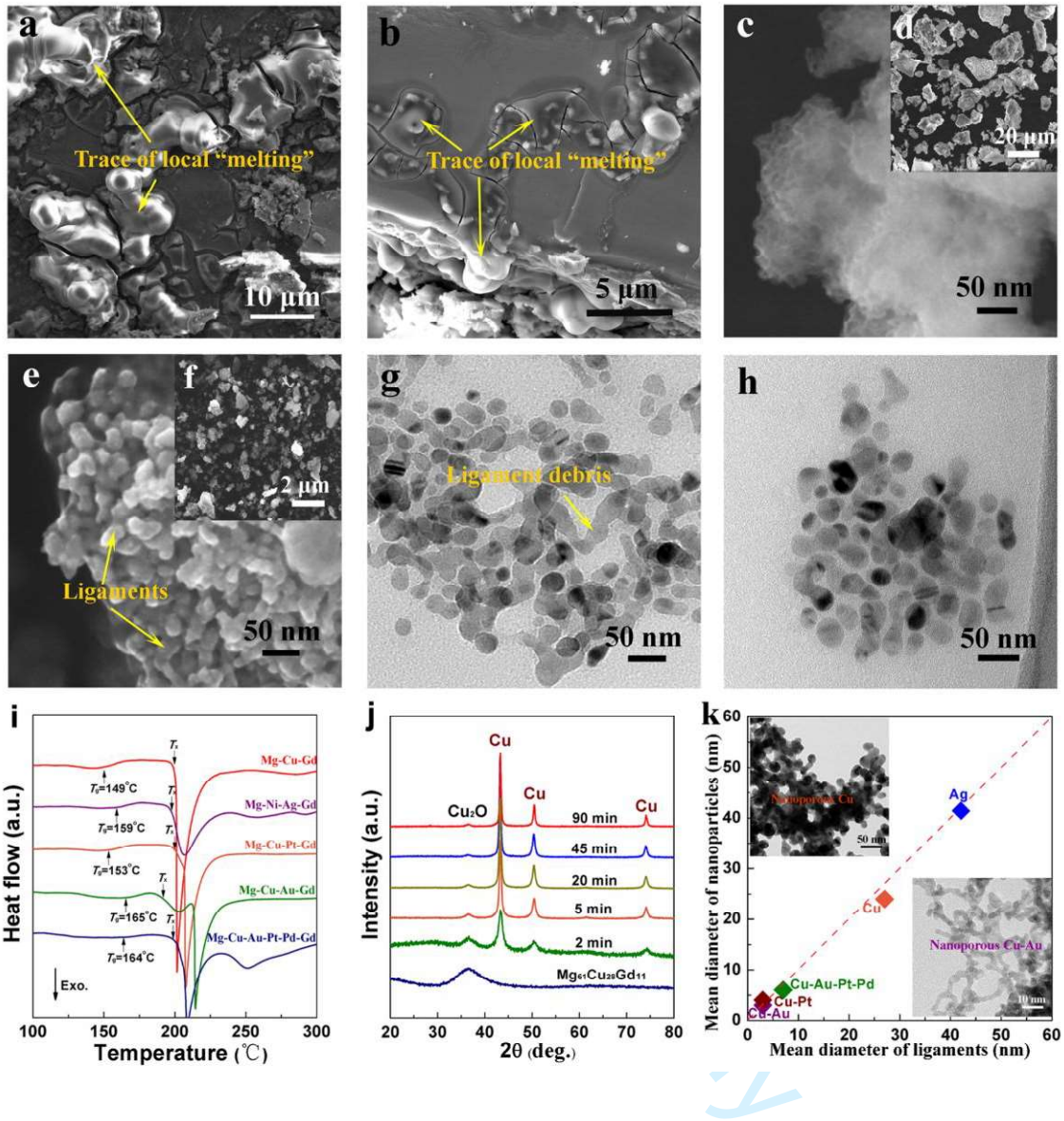
a
Trace of local "melting"
10 μm
b
Trace of local "melting"
5 μm
c
d
20 μm
50 nm
e
f
2 μm
Ligaments
50 nm
g
Ligament debris
50 nm
h
50 nm
i
Heat flow (a.u.)
Mg-Cu-Gd
Mg-Ni-Ag-Gd
Mg-Cu-Pt-Gd
Mg-Cu-Au-Gd
Mg-Cu-Au-Pt-Pd-Gd
Exo.
Temperature (℃)
j
Cu
Cu₂O
Cu
Cu
90 min
45 min
20 min
5 min
2 min
Mg₆₁Cu₂₈Gd₁₁
Intensity (a.u.)
2θ (deg.)
k
Mean diameter of nanoparticles (nm)
Mean diameter of ligaments (nm)
Ag
Cu
Cu-Au-Pt-Pd
Cu-Pt
Cu-Au
Nanoporous Cu-Au

Figure 4

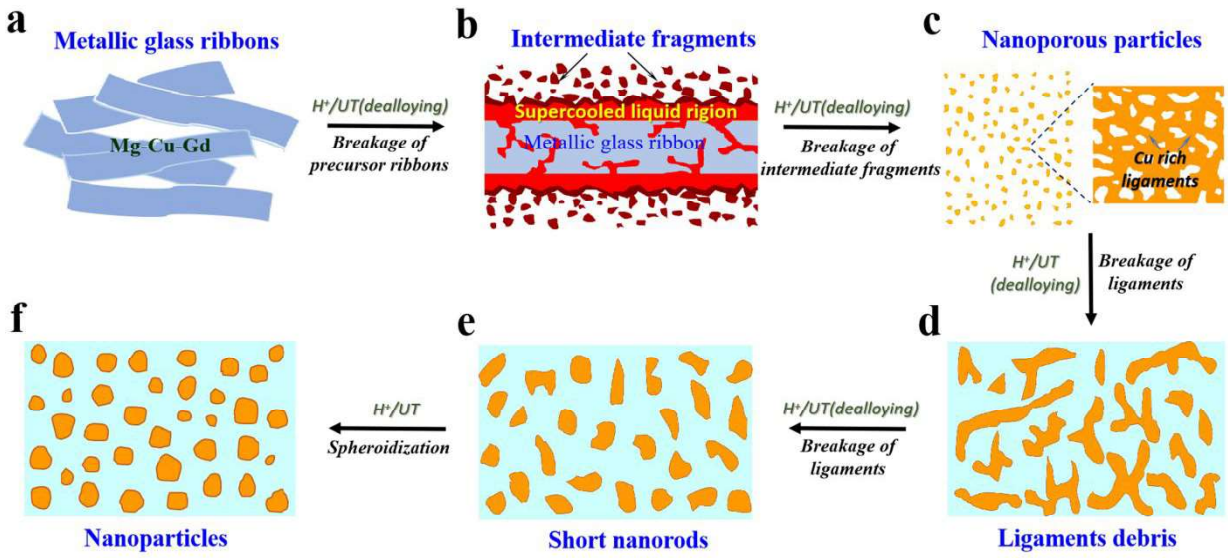

Figure 5

Supporting Information

Facile synthesis of metal and alloy nanoparticles by ultrasound-assisted dealloying of metallic glasses

Yuan-Yun Zhao [1, 2, 5], Feng Qian [2, 4], Wenfeng Shen [3], Chengliang Zhao [1, 5], Jianguo Wang [1, 5], Chunxiao Xie [1,5], Fengling Zhou [1], Chuntao Chang [1, 5*], Yanjun Li [2, *]

[1]*Neutron Scattering Technical Engineering Research Center, School of Mechanical Engineering, Dongguan University of Technology, Dongguan 523808, China*

[2]*Department of Materials Science and Engineering, Norwegian University of Science and Technology, Trondheim 7491, Norway*

[3]*Ningbo Institute of Materials Technology and Engineering, Chinese Academy of Sciences, Ningbo 315201, China*

[4]*School of Materials Science and Engineering, Beijing Institute of Technology, 100081, Beijing, China*

[5]*Guangdong-Hong Kong-Macao Joint Laboratory for Neutron Scattering Science and Technology, Dongguan University of Technology, Dongguan, 523808, China*

[*]Corresponding authors.

Email address: changct@dgut.edu.cn (C.T. Chang); yanjun.li@ntnu.no (Y.J. Li)

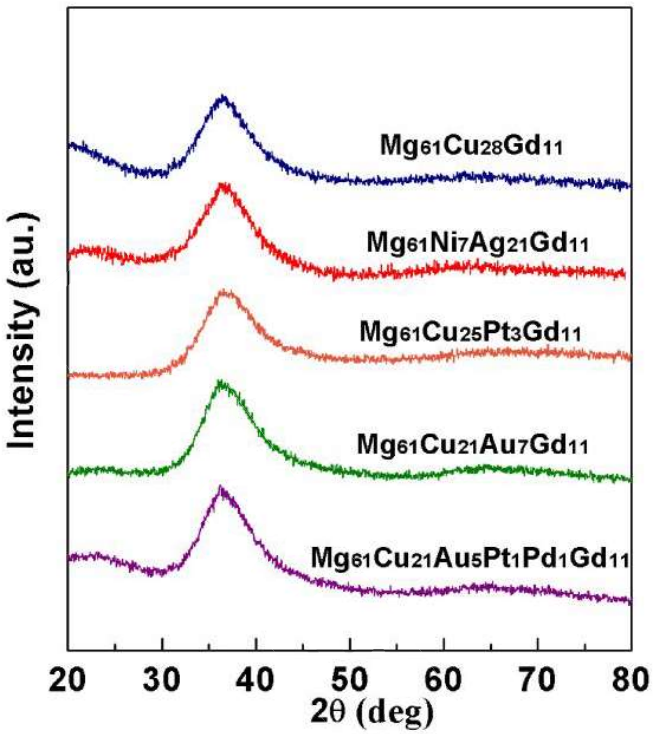

Supplementary Fig. 1. XRD spectra of the $Mg_{61}Cu_{28}Gd_{11}$, $Mg_{61}Ni_7Ag_{21}Gd_{11}$, $Mg_{61}Cu_{25}Pt_3Gd_{11}$, $Mg_{61}Cu_{21}Au_7Gd_{11}$, and $Mg_{61}Cu_{21}Au_5Pt_1Pd_1Gd_{11}$ metallic glass ribbons with thicknesses of ~30 μm.

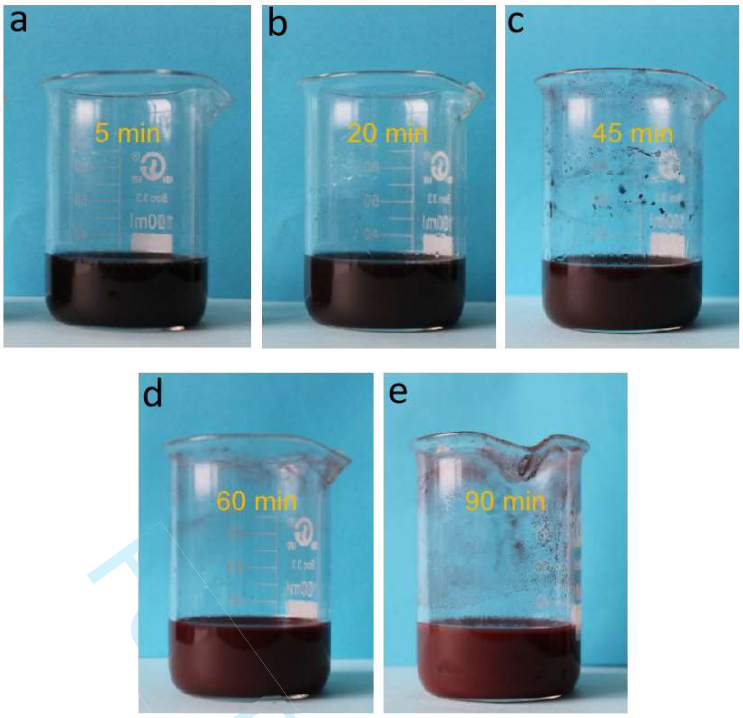

Supplementary Fig. 2. Photographs of the reaction solution by ultrasound-assisted dealloying of 0.25 g $Mg_{61}Cu_{28}Gd_{11}$ metallic glass ribbons in 30 ml of 0.24 mol L^{-1} HCl/ethanol solution for 5 min (a), 20 min (b), 45 min (c), 60 min (d), and 90 min (e).

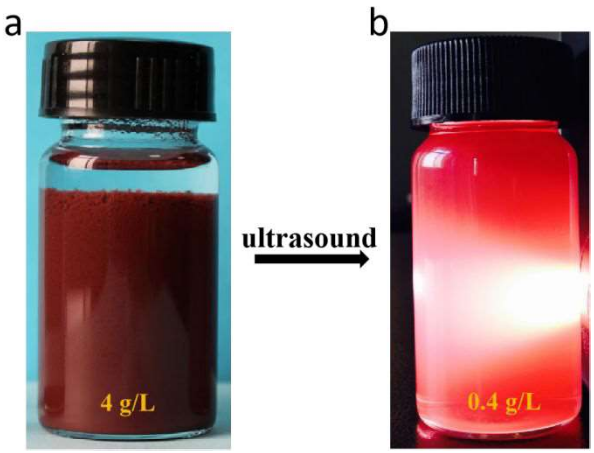

Supplementary Fig. 3. (a) Photographs of the soft aggregated colloidal Cu nanoparticles (4 g L^{-1}, after standing for 5 h); (b) Photographs of the Tyndall effect of a dilute Cu nanoparticles colloidal solution (0.4 g L^{-1}, after standing for 1 h) prepared by re-dispersing the soft aggregated colloidal Cu nanoparticles in (a).

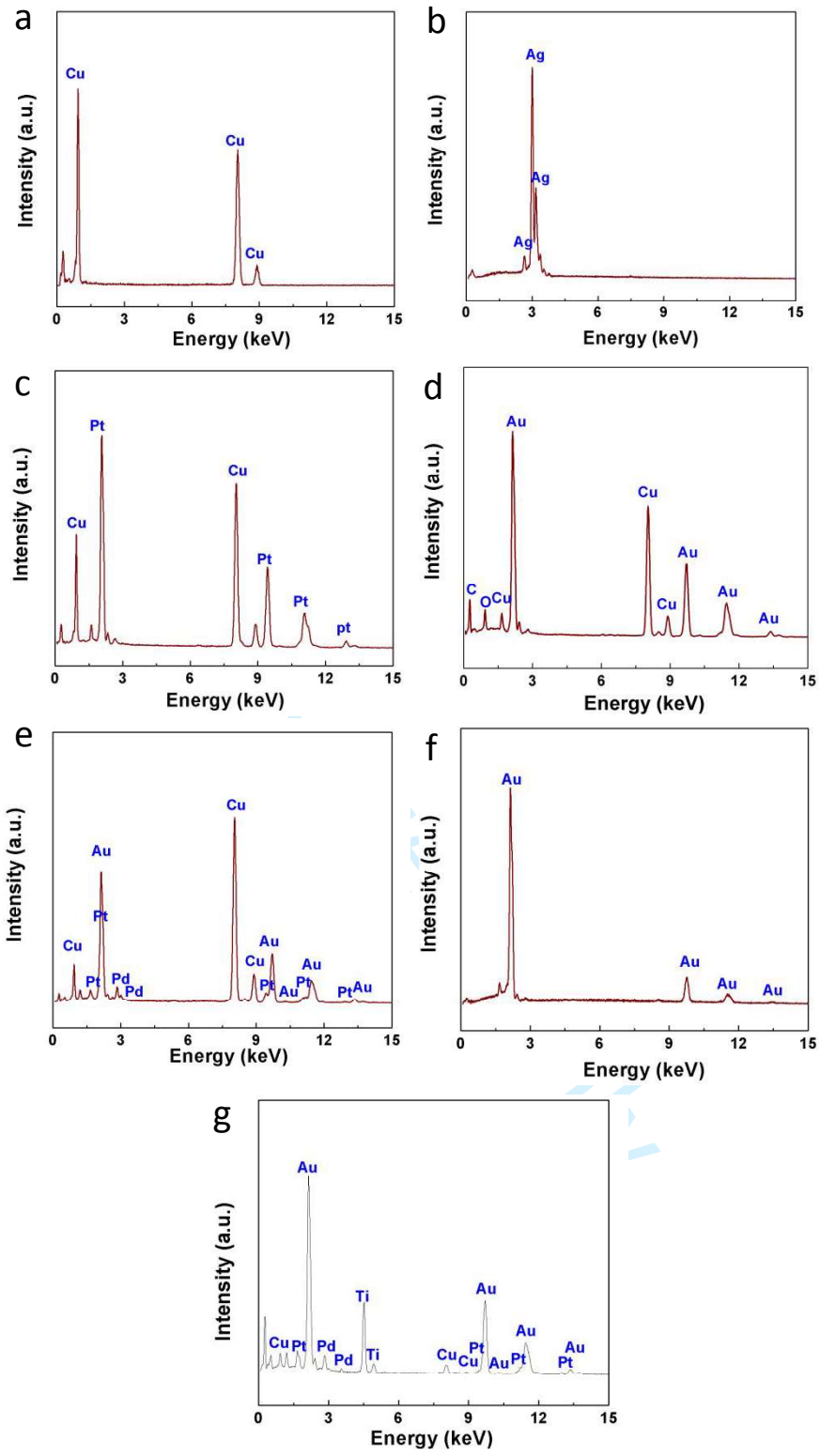

Supplementary Fig. 4. The energy dispersive spectrometer (EDS) spectra of the Cu (a), Ag (b), Cu-Pt (c), Cu-Au (d), Cu-Au-Pt-Pd (e), Au (f), and Au-Pt-Pd-Cu (g) nanoparticles. The Ti signal is due to the titanium grid specimen holder.

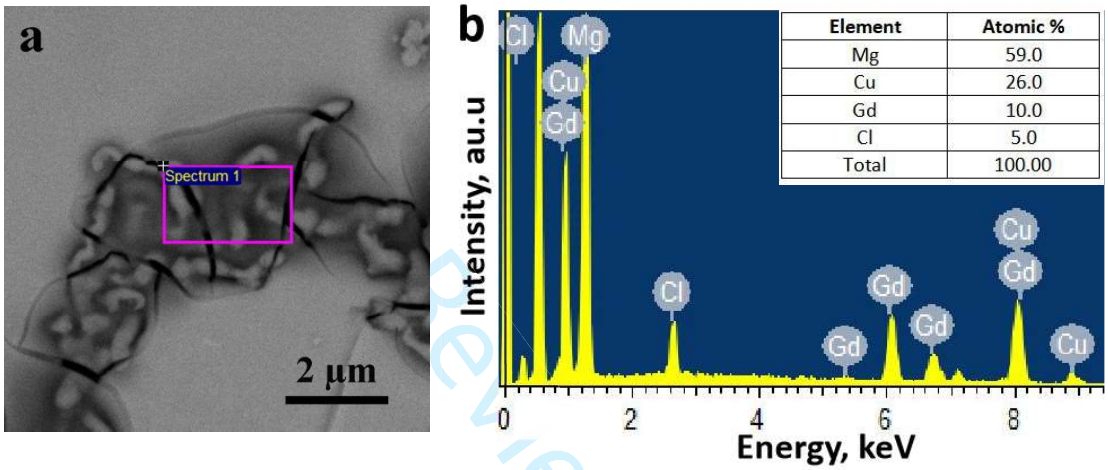

Supplementary Fig. 5. (a) Electron back-scattered diffraction (EBSD) image, and (b) EDS result of the local "melted" area in the interior of the remaining $Mg_{61}Cu_{28}Gd_{11}$ metallic glass ribbon after dealloying for 2 min.

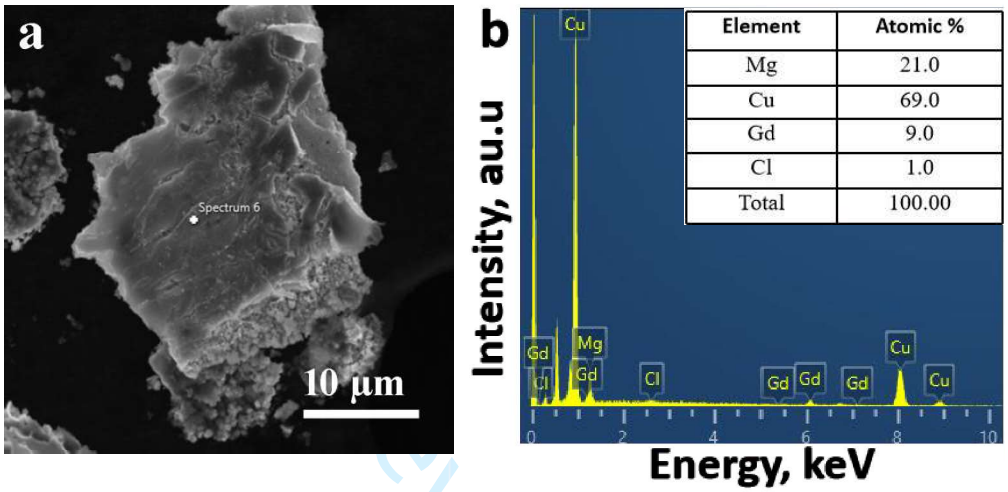

Supplementary Fig. 6. (a) SEM and (b) EDS results of the intermediate fragments after dealoying for 2 min.

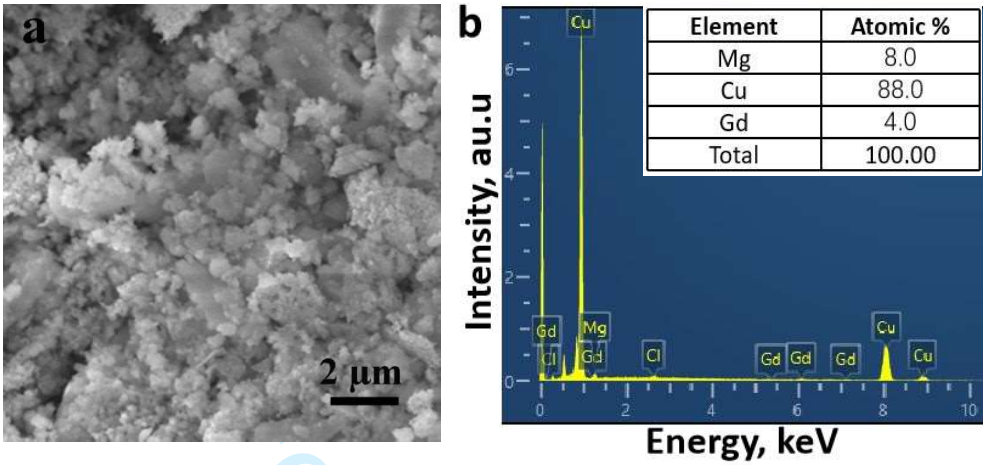

Supplementary Fig. 7. (a) SEM and (b) EDS results of the small nanoporous particles after dealoying for 5 min.

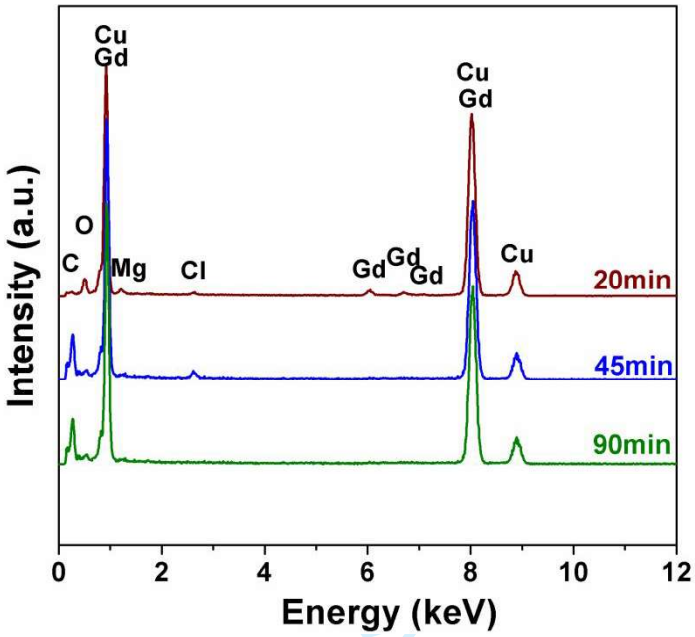

Supplementary Fig. 8. EDS spectra of the intermediate products at a reaction time of 20 min, 45 min, and 90 min by ultrasound-assisted dealloying of $Mg_{61}Cu_{28}Gd_{11}$ metallic glass ribbons.

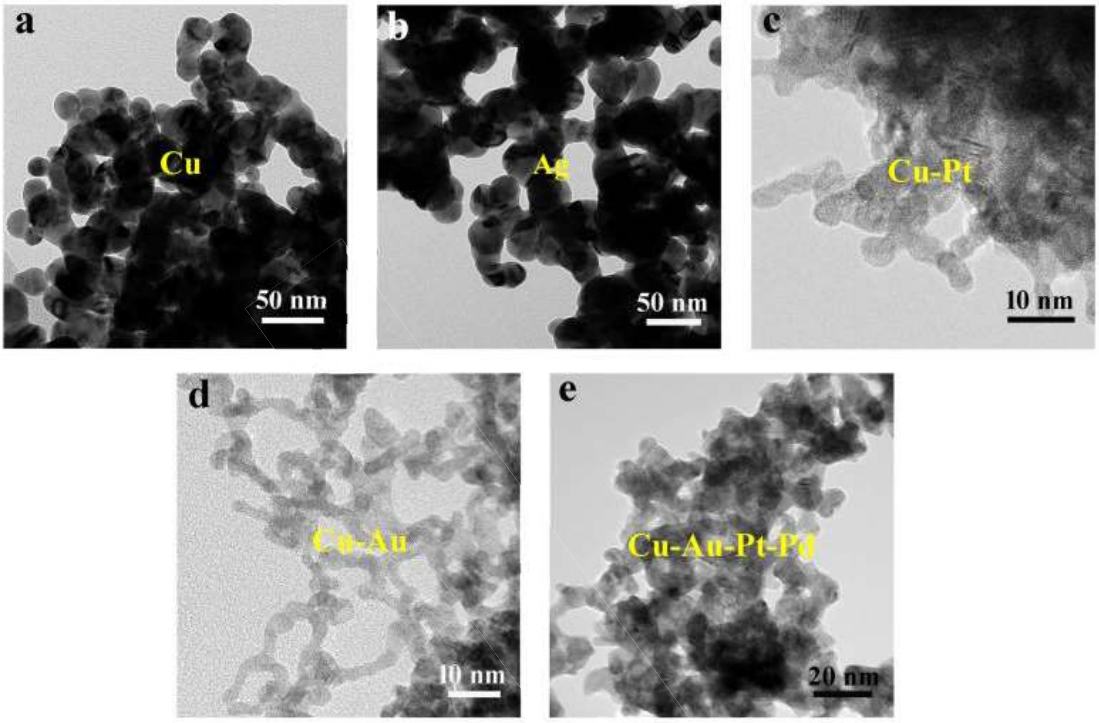

Supplementary Fig. 9. TEM images of the nanoporous metals by ordinary dealloying (without UT) of $Mg_{61}Cu_{28}Gd_{11}$ (a), $Mg_{61}Ni_7Ag_{21}Gd_{11}$ (b), $Mg_{61}Cu_{25}Pt_3Gd_{11}$ (c), $Mg_{61}Cu_{21}Au_7Gd_{11}$ (d), and $Mg_{61}Cu_{21}Au_5Pt_1Pd_1Gd_{11}$ (e) metallic glass ribbons.

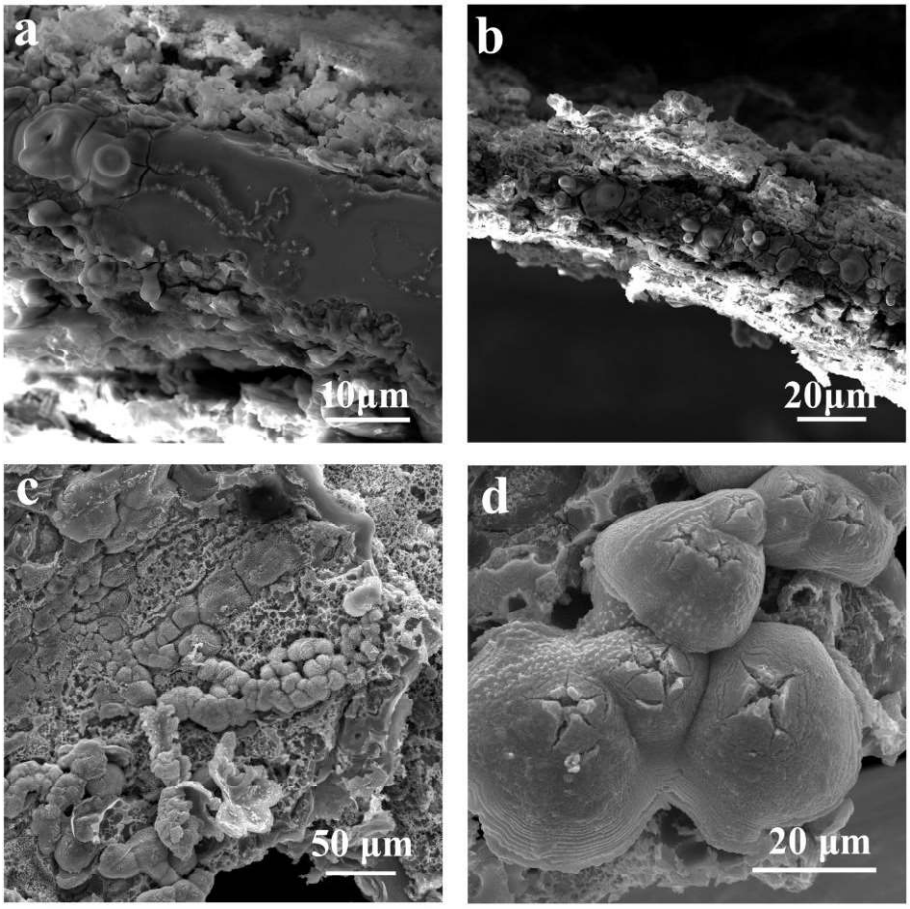

Supplementary Fig. 10. SEM images of the intermediate products by ordinary dealloying (without UT) of $Mg_{61}Cu_{28}Gd_{11}$ metallic glass ribbons in 0.24 mol L^{-1} HCl/ethanol solution for 5 min (a), 8 min (b), and 30 min (c-d). Due to a low viscosity (η=10^6-10^8 Pa s) of the as-formed supercooled liquid phase, the bulging effect of in-situ generated H_2 on the supercooled liquid phase occurred not only on the surface regions but also in some interior regions of the precursor ribbons. The traces of the flowed supercooled liquid phase and the H_2 escape sites can be seen in (d). In order to demonstrate the traces of flowed supercooled liquid phase more obviously, the thickness of the metallic glass ribbons in (c) and (d) is ~100 μm.

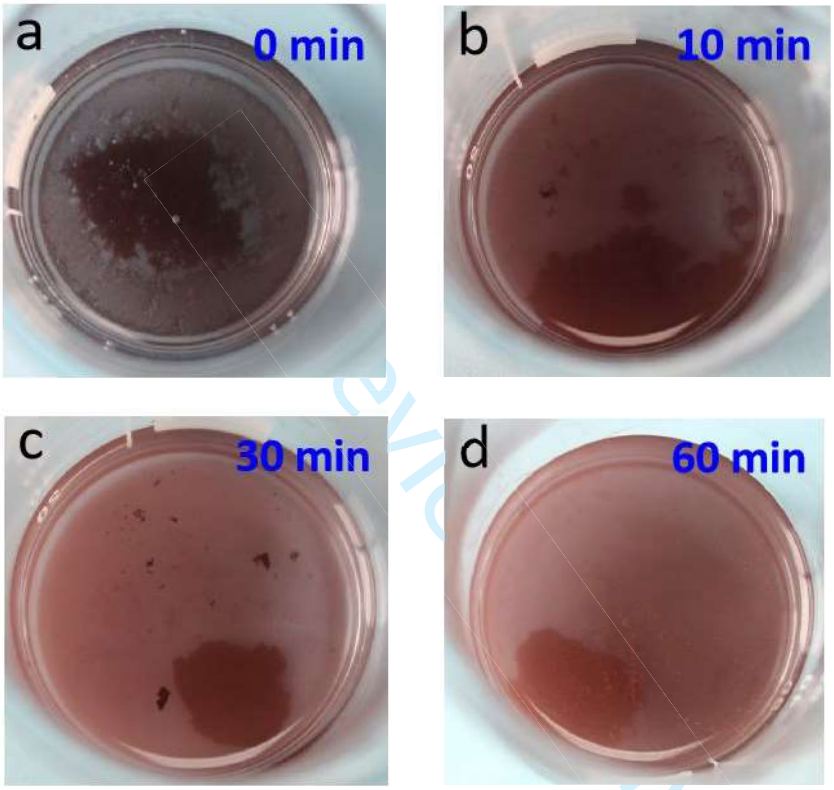

Supplementary Fig. 11. (a) Photograph of the as-prepared nanoporous Cu by ordinary dealloying of $Mg_{61}Cu_{28}Gd_{11}$ metallic glass ribbons in 30 ml 0.24 mol/L HCl/ethanol solution for 90 min (without UT). Due to the bulging effect of in-situ generated H_2 on the dealloying precursor ribbons, the final products are large nanoporous Cu particles, which do not keep their original ribbon shape. (b) Ordinary dealloying for 90 min + UT for 10 min, (c) Ordinary dealloying for 90 min + UT for 30 min, (d) Ordinary dealloying for 90 min + UT for 60 min.

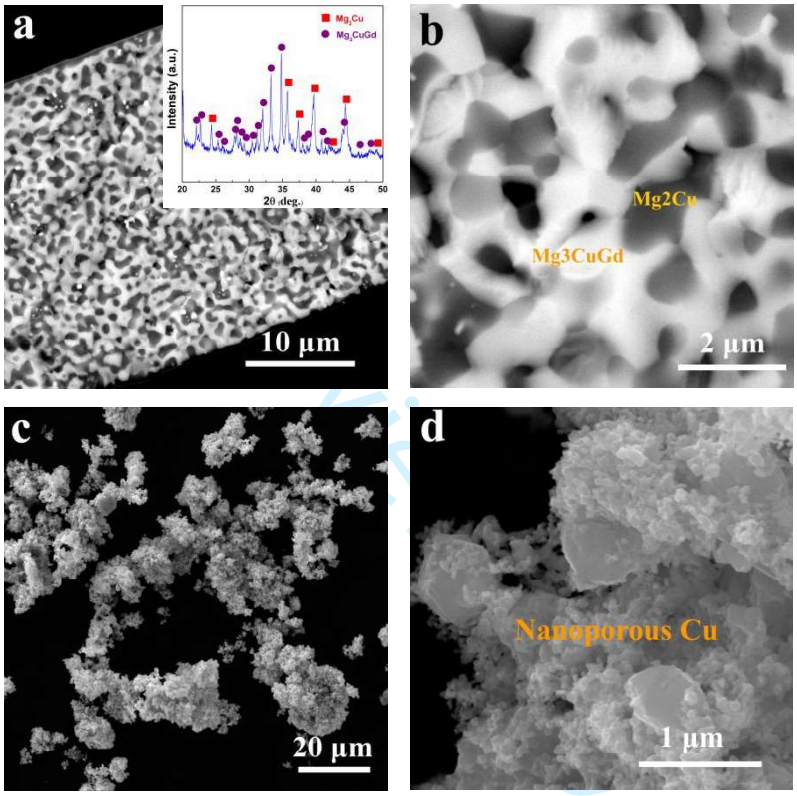

Supplementary Fig. 12. (a-b) BSEM images of the crystallized $Mg_{61}Cu_{28}Gd_{11}$ ribbon (the insert shows the XRD spectrum). (c-d) SEM images of the as-prepared nanoporous Cu particles by ultrasound-assisted dealloying of crystallized $Mg_{61}Cu_{28}Gd_{11}$ alloy ribbons in 0.24 mol L^{-1} HCl/ethanol solution for 90 min. The nanoporous Cu with different morphology in (d) is correspond to different dealloying products of Mg_2Cu phase and Mg_3CuGd phase in (b).

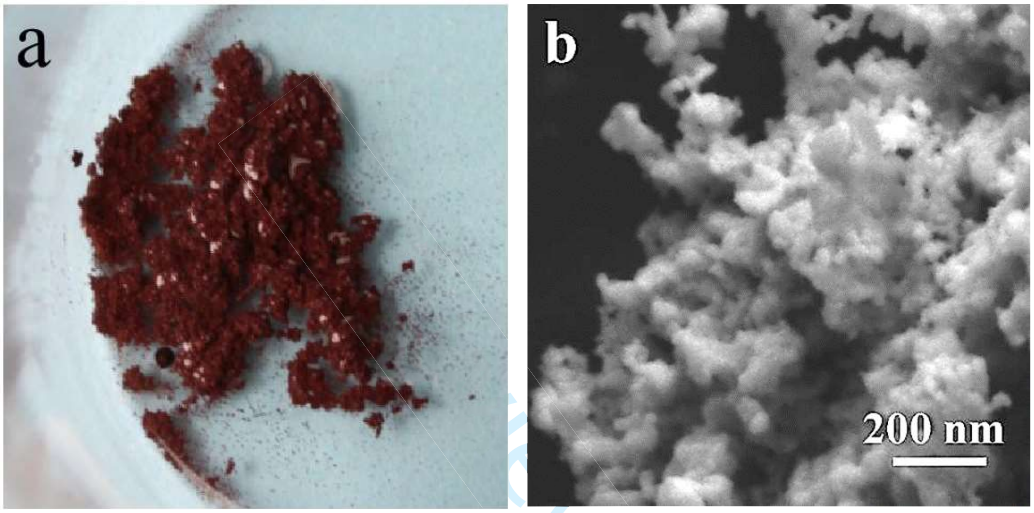

Supplementary Fig. 13. (a) Photograph and (b) SEM image of the as-prepared nanoporous Cu by ultrasonic-assisted dealloying of $Mg_{61}Cu_{28}Gd_{11}$ metallic glass ribbons in 0.24 mol L^{-1} HCl/water solution for 90 min.

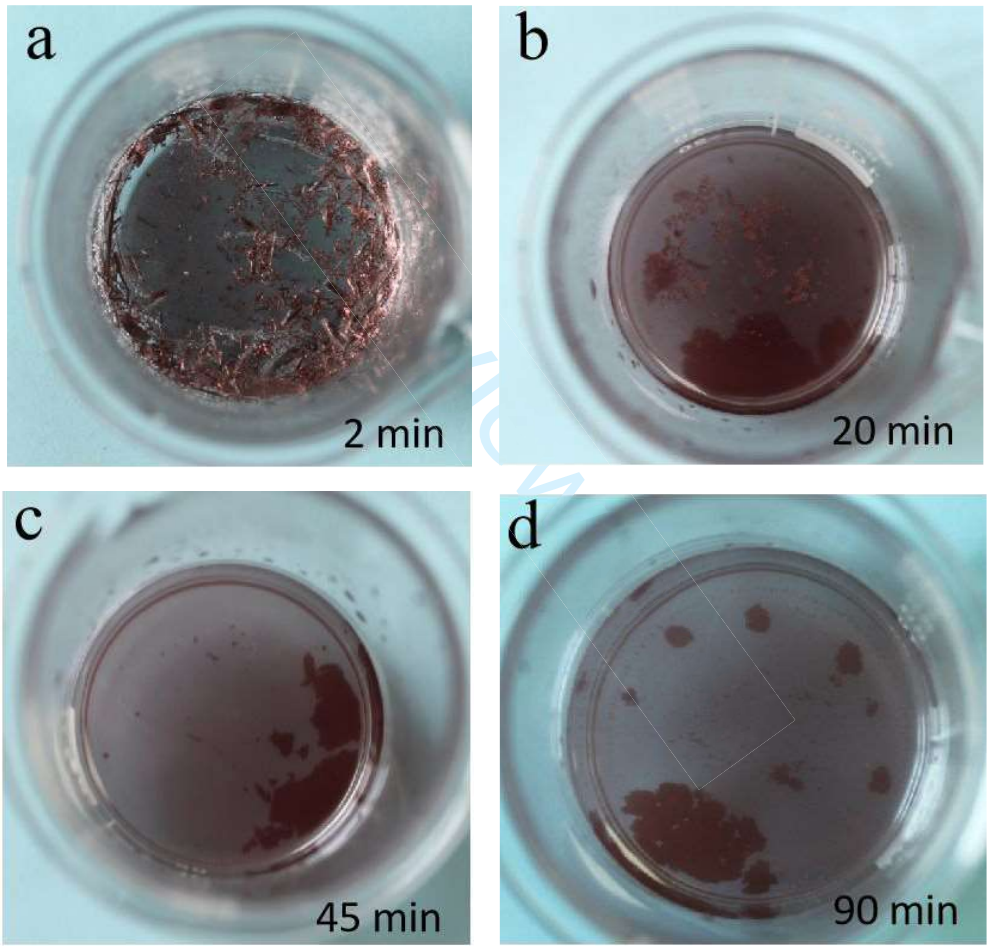

Supplementary Fig. 14. Photograph of the as-prepared nanoporous Cu by ultrasonic-assisted dealloying of $Mg_{61}Cu_{28}Gd_{11}$ metallic glass ribbons in 0.12 mol L^{-1} H_2SO_4/water solution for 2 min (a), 20 min (b), 45 min (c), and 90 min (d).